International Journal of Heat and Mass Transfer 95 (2016) 249–263

Contents lists available at ScienceDirect

International Journal of Heat and Mass Transfer

journal homepage: www.elsevier.com/locate/ijhmt

Experimental and computational investigation of vertical upflow condensation in a circular tube

Chirag R. Kharangate, Hyoungsoon Lee, Ilchung Park, Issam Mudawar *

Purdue University Boiling and Two-Phase Flow Laboratory (PU-BTPFL), School of Mechanical Engineering, 585 Purdue Mall, West Lafayette, IN 47907, USA

ARTICLE INFO

Article history:
Received 29 September 2015
Received in revised form 2 November 2015
Accepted 4 November 2015
Available online 21 December 2015

Keywords:
Flow condensation
Phase change
Vertical upflow
Computational FLUENT model

ABSTRACT

This study explores the condensation of FC-72 in vertical upflow both experimentally and computationally. An axisymmetric 2-D computational model is used to predict variations of void fraction, condensation heat transfer coefficient, wall temperature and temperature profile across the liquid film. The computed results are shown to effectively capture the observed complex flow characteristics during flooding and climbing film conditions, including the annular film's interfacial waviness, formation of liquid ligaments along the film's interface, and breakup of liquid masses from these ligaments that are either re-deposited onto the film or entrained in the vapor core before moving towards the centerline. The model also shows good agreement with measured spatially averaged condensation heat transfer coefficients and wall temperatures. The predicted temperature profiles across the flow area successfully capture an appreciable temperature gradient at the liquid–vapor interface and saturation temperature in the vapor core.

1. Introduction

1.1. Phase change methods for thermal management applications

The past three decades have witnessed unprecedented increases in the amount of the heat that must be removed from heat dissipating devices and systems, including computer data centers, electric vehicle power electronics, avionics, and directed energy laser and microwave weapon systems [1]. Coupled with stringent weight and volume constraints, the increased rate of heat dissipation meant that conventional single-phase air-cooled or liquid-cooled thermal management systems could no longer safely achieve the heat removal requirements. Through their ability to capitalize upon latent heat content in addition to sensible heat, phase change thermal management systems are ideally suited for high heat density applications. With their ability to increase boiling and condensation heat transfer coefficients by orders of magnitude compared to liquid-cooled systems, phase change systems greatly reduce surface temperatures, and therefore increase the life of both device and system.

The vast majority of recent studies concerning two-phase thermal management have been focused on heat acquisition through evaporation or boiling, while the number of studies addressing heat rejection by condensation is relatively small. And most of the published condensation studies concern vertical downflow, a flow orientation that provides fairly stable condensate film motion aided by gravity. This configuration was explored in great detail by Park et al. [2] both experimentally and theoretically. However, because of volume and packaging constraints, it is impractical to design condensers utilizing the vertical downflow orientation alone. Most condensers adopt a serpentine design, with flow often alternating between vertical downflow and vertical upflow. Therefore, understanding vertical upflow condensation is crucial for the design of condensers used in two-phase thermal management systems.

Vertical upflow condensation is substantially more complicated than vertical downflow because of the opposing influences of vapor shear and gravity on the motion of the condensate film. As indicated in [3], several distinct flow regimes are encountered in vertical upflow condensation. At low inlet flow rates, the liquid film is driven downwards by gravity as the upward vapor shear is too weak to influence the film's motion; this flow behavior is categorized as the *falling film* regime. Increasing the flow rate causes the flow to transition to an *oscillating film* regime, corresponding to the liquid film alternating between upflow and downflow. A further increase in flow rate results in *flooding*, where vapor shear becomes strong enough to just balance the weight of the liquid film, causing the film to begin its ascent. Further flow rate

* Corresponding author. Tel.: +1 (765) 494 5705; fax: +1 (765) 494 0539.
E-mail address: mudawar@ecn.purdue.edu (I. Mudawar).
URL: https://engineering.purdue.edu/BTPFL (I. Mudawar).

http://dx.doi.org/10.1016/j.ijheatmasstransfer.2015.11.010
0017-9310/

Nomenclature

Δc	mesh (cell) size
c_p	specific heat at constant pressure
c_v	specific heat at constant volume
D	diameter
$e_{i,j}$	strain rate tensor
E	specific internal energy (J/kg)
F	force
G	mass velocity (kg/m^2 s)
g	gravitational acceleration
h	heat transfer coefficient
h_{fg}	latent heat of vaporization
I	turbulence intensity
k	thermal conductivity
L	condensation length used in computational model
M	molecular weight
$\dot{m}$	mass flow rate
$\dot{m}''$	interfacial mass flux
$\vec{n}$	unit vector normal to interface
p	pressure
Q	energy source term (W/m^3)
q''	heat flux
R	universal gas constant (=8.314 J/mol K)
R_1, R_2	radii of curvature at free interface
Re	Reynolds number
r_i	mass transfer intensity (s^{-1})
S	volumetric mass source (kg/m^3 s)
T	temperature
t	time
t_i	unit tangential vector on free interface
U	velocity
u	velocity
x_e	thermodynamic equilibrium quality
y	distance perpendicular to the wall
y^+	dimensionless distance perpendicular to the wall
z	stream-wise coordinate
z_0	axial location where $x_e = 1$

Greek symbols

α	volume fraction; void fraction
γ	molecules transfer fraction in Schrage model [48]
δ_i	initial assumed liquid film thickness
μ	dynamic viscosity
ρ	density
σ	surface tension
τ	time period ($L/U_{g,in}$)

Superscripts

–	time average
$\rightarrow$	vector
‘	fluctuating component
+	dimensionless

Subscripts

avg	spatial average
c	condensation
e	evaporation, thermodynamic equilibrium
eff	effective
f	liquid
g	vapor
h	hydraulic
i	initial, interfacial, thermocouple location, direction index
in	inlet
j	direction index
k	phase
sat	saturation
vol	volume
w	water
wall	wall

increases cause the vapor shear to overcome gravity effects and the liquid film to flow upwards; this behavior is categorized as the *climbing film* regime.

1.2. Predictive methods for condensation

In general, condensing flows encompass a variety of regimes including pure vapor, annular, slug, bubbly and pure liquid [4], which occur in order of decreasing quality. Given the vast differences in interfacial behavior among these regimes, it is quite difficult to construct universal models for flow condensation. This is why flow regime maps and/or models are constructed for condensing flows [5–8], which serve as a logical starting point for constructing models that are specific to individual regimes.

Of the aforementioned regimes, annular flow has received the most attention by researchers because of its prevalence over the largest fraction of the length of a condensation tube. Such studies include semi-empirical correlations, which are limited in validity to the ranges of parameters used in the database upon which a correlation is based [9–20]. A second approach to predicting annular condensation in tubes is the predominantly theoretical control-volume-based method [21]. The third, and rather more recent approach, is computational modeling [22–25]. Numerical simulations can be used to predict flow behavior with velocity profiles and turbulence structures, as well as parameters that can be measured experimentally, such as heat transfer coefficient. A key advantage of computational models is their ability to predict transient behavior, which is absent from correlations or theoretical models.

1.3. Numerical methods for multi-phase flows

Numerical approaches for multiphase system can be grouped into three general categories: Lagrangian, Eulerian, and Eulerian–Lagrangian. The Lagrangian approach involves tracking a portion of the fluid or interface and observing how it behaves. Smoothed-Particle Hydrodynamics (SPH) [26,27] and Particle-in-Cell (PIC) [28] methods have been adopted in conjunction with the Lagrangian approach. Due to the need for complicated grip topologies, the Lagrangian approach has been limited to rather simple flow situations.

The Eulerian approach is simpler and easier to implement, which explains its popularity relative to the Lagrangian approach. The Level-set Method (LSM) [29] and Volume of Fluid (VOF) method [30] are two schemes that have been developed in conjunction with the Eulerian approach. The LSM is capable of capturing curvatures and sharp interfaces accurately, but has issues preserving mass conservation. The VOF method [30] is based on the phase volume fraction, α, of each phase, which has a value between 0 and 1. While this method preserves mass conservation along the interface, it is less accurate than the LSM in determining interface topology. The Coupled Level-Set/Volume of Fluid (CLSVOF) method is based on the LSM, but also employs the VOF method to conserve mass when the interface is advected [31–33].

The third approach combines Eulerian and Lagrangian perspectives. Unverdi and Tryggvason [34] and Tryggvason et al. [35] used this combined Eulerian–Lagrangian approach, which is called the Front Tracking method. This method uses a fixed grid with a moving grid adopted at the interface to take advantage of both the Eulerian and Lagrangian perspectives.

While annular upflow condensation is the specific focus of the present study, recent efforts at the Purdue University Boiling and Two-Phase Flow Laboratory (PU-BTPFL) have been focused on developing predictive tools to tackle interfacial complexities in a number of important phase-change configurations, including heated and evaporating falling films [36,37], critical heat flux in pool boiling [38], flow boiling [39–41], jet-impingement [42,43] and sprays [44,45].

1.4. Phase change models for interfacial mass transfer

Computational modeling of flow condensation requires an appropriate mass transfer model. Three common mass transfer models have been used in the literature. The first model is based on the Rankine–Hugoniot jump condition [46] for energy conservation at the interface. It neglects micro-scale mass transfer, and saturation temperature is manually maintained at the interface. The mass transfer rate is determined from energy conservation at the interface according to the relation

$$q_i'' = -k_{eff}\nabla T_i \cdot \vec{n} = \dot{m}'' h_{fg}, \tag{1}$$

where $\dot{m}''$ (kg/m^2 s) is the mass flux due to phase change at the interface. The volumetric mass source term, S (kg/m^3 s), for the individual phases is determined from

$$S_g = -S_f = \dot{m}''|\nabla \alpha_g| = \frac{k_{eff}(\nabla\alpha \cdot \nabla T)}{h_{fg}}, \tag{2}$$

where k_{eff} is the effective thermal conductivity determined from the volume fractions and thermal conductivities of the liquid and vapor. In effect, this model assumes all the energy crossing the interface is consumed by mass transfer.

The second model is based on the Hertz–Knudsen equation [47], first developed by Schrage [48], which allows for interfacial jumps in temperature and pressure, where $T_{sat}(p_f) = T_f \neq T_{sat}(p_g) = T_g$. The net mass flux across the interface, $\dot{m}''$ (kg/m^2 s), is determined by the difference between the liquid-to-vapor and vapor-to-liquid mass fluxes,

$$\dot{m}'' = \frac{2}{2-\gamma_c}\sqrt{\frac{M}{2\pi R}}\left[\gamma_c \frac{p_g}{\sqrt{T_g}} - \gamma_e \frac{p_f}{\sqrt{T_f}}\right], \tag{3}$$

where R = 8.314 J/mol K is the universal gas constant, γ the fraction of molecules transferred from one phase to the other during phase change, and $1-\gamma$ the fraction of molecules reflected at the interface. The subscripts c and e in Eq. (3) refer to condensation and evaporation, respectively, and $\gamma_e = 1$ represents complete evaporation and $\gamma_c = 1$ complete condensation [49]. Many investigators use equal values for γ_c and γ_e by setting $\gamma_c = \gamma_e = \gamma$ in phase change simulations, and refer to γ as the "accommodation coefficient." By setting the interfacial temperature equal to T_{sat}, and assuming the heat flux is linearly dependent on temperature jump between the interface and the vapor, Tanasawa [50] simplified Eq. (3) to obtain a modified net mass flux as

$$\dot{m}'' = \frac{2\gamma}{2-\gamma}\sqrt{\frac{M}{2\pi R}}\frac{\rho_g h_{fg}(T - T_{sat})}{T_{sat}^{3/2}}, \tag{4}$$

where T_{sat} is based on local pressure, p, and the volumetric mass source term is determined from

$$S_g = -S_f = \dot{m}''|\nabla \alpha_g|. \tag{5}$$

This model is applicable only to the liquid–vapor interface, and has been used mostly to tackle evaporating films, condensing films, and film boiling.

Lee [51] proposed a third model that has been widely used in recent flow condensation studies [23–25]. This model is based on the assumption that mass is transferred at a constant pressure and a quasi thermo-equilibrium state, and obtained from the relations

$$S_g = -S_f = r_i \alpha_g \rho_g \frac{(T - T_{sat})}{T_{sat}} \quad \text{for condensation } (T < T_{sat}) \tag{6a}$$

and

$$S_g = -S_f = r_i \alpha_f \rho_f \frac{(T - T_{sat})}{T_{sat}} \quad \text{for evaporation } (T > T_{sat}), \tag{6b}$$

where r_i is an empirical coefficient called the "mass-transfer intensity factor" and has the units of s^{-1}.

1.5. Objectives of study

This study will explore both experimentally and computationally the complex interfacial behavior associated with annular upflow condensation in a vertical circular tube. The computational model will also be used to explore both local and spatially averages of both the heat transfer coefficient and wall temperature. Aside from validating the model against experimental measurements, the phase change model incorporated in the computational model is validated by its ability to capture both saturation temperature in the vapor core and temperature gradient at the liquid–vapor interface.

2. Experimental methods

The data used to assess the accuracy of the computational model are obtained using the PU-BTPFL flow condensation facility depicted in Fig. 1(a). Fig. 1(b) provides a schematic of the flow loop that is used to supply FC-72 vapor to the condensation module. The system consists of three flow loops, a primary FC-72 condensation loop and two water cooling loops. Heat is extracted from the FC-72 first via the condensation module utilizing the first water loop, and again via a separate condenser utilizing the second water loop. Two separate FC-72 condensation modules are used, both utilizing tube-in-tube construction, and within which the FC-72 vapor is condensed by rejecting heat to water that is supplied in counterflow.

Illustrated schematically in Fig. 2(a), the first condensation module is used for heat transfer measurements. Superheated FC-72 vapor is supplied through the inner 304 stainless steel tube and is cooled by water supplied in counterflow through the outer annulus. The inner tube has an 11.89-mm i.d. and wall thickness of 0.41 mm, while the outer tube, also made from 304 stainless steel, has a 22.48-mm i.d. This module features a condensation length of 1259.8 mm. The small wall thickness of the inner tube, coupled with the relatively low thermal conductivity of stainless steel, is intended to minimize axial conduction along the condensation length. Two sets of diametrically opposite type-T thermocouples are attached to the outer surface of the inner tube at 14 axial locations to measure the outer wall temperature. The water temperature is also measured at the same 14 different axial locations. FC-72 pressure is measured at the inlet and outlet of the condensation length. The operating conditions for the condensation module used for heat transfer measurements are provided in Table 1. These are the same conditions used in the computational model.

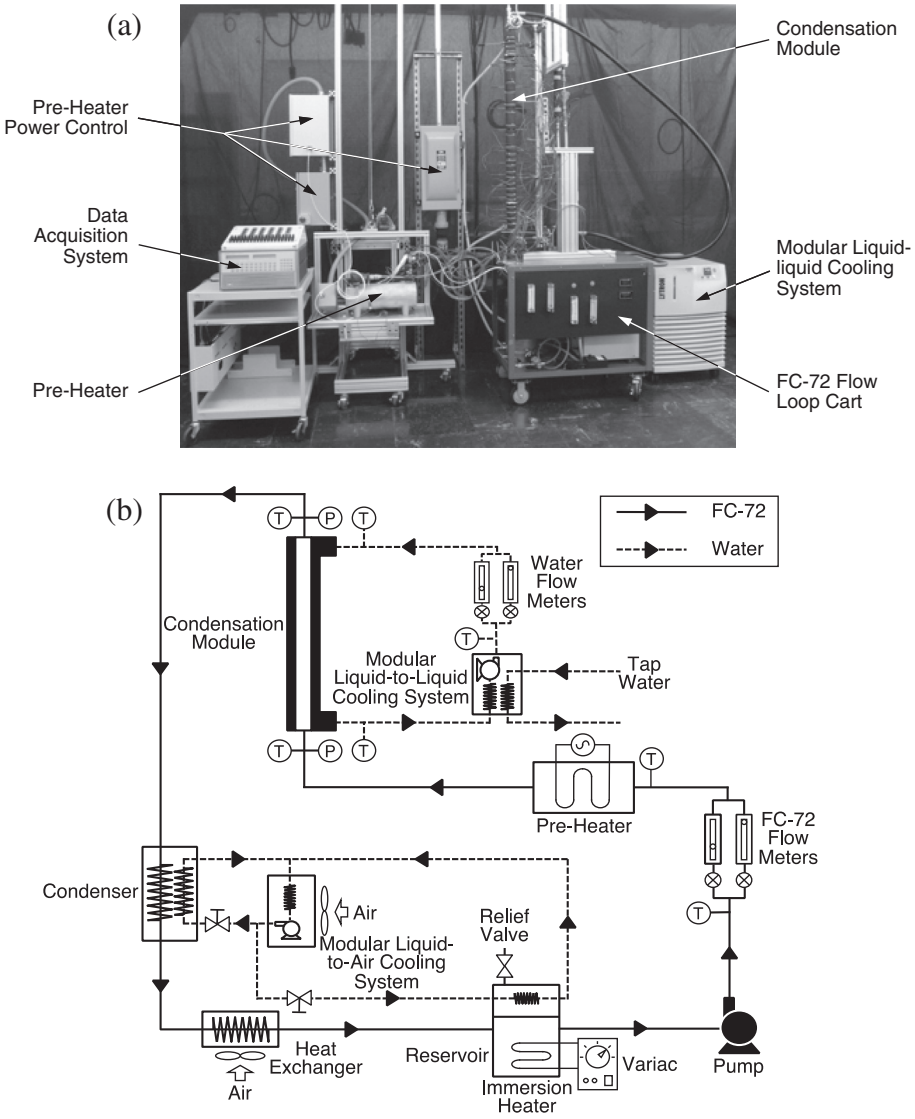

Fig. 1. (a) Photo of condensation facility. (b) Schematic of flow loop.

Shown in Fig. 2(b), the flow visualization module also features a tube-in-tube construction, with the FC-72 flowing through the inner tube and water through the outer annulus. The inner borosilicate glass tube has a 10.16-mm i.d. and a wall thickness of 1.8 mm. The outer polycarbonate (Lexan) plastic tube has an inner diameter of 19.05 mm. This module features a condensation length of 1219.0 mm. The inlets and outlets for the FC-72 and water are fitted with Type-T thermocouples and pressure transducers. Flow visualization is achieved with the aid of a high-speed Photron Fastcam Ultima APX video camera system.

3. Computational methods

3.1. Governing equation

The present study employs the standard two-equation $k-\omega$ turbulence model with shear stress transport (SST) formulation as prescribed in the ANSYS Guide [52], and using a turbulence dampening factor of 10. The methodology used here is similar to that adopted in a recent computational model of evaporating falling films by Kharangate et al. [53] that was proven highly effective at capturing interfacial phase change. The VOF method in FLUENT is used to compute the conservation equations for both liquid and vapor, and also to account for mass transfer between the phases. The continuity equations are expressed as

$$\frac{\partial}{\partial t}(\alpha_k \rho_k) + \nabla.(\alpha_k \rho_k u_k) = S_k, \tag{7}$$

where subscript k refers to either liquid, f, or vapor, g, and S (kg/m^3 s) is the volumetric mass source term due to phase change. The momentum and energy equations applied to the combined phases are given, respectively, by

$$\frac{\partial}{\partial t}(\rho\vec{u}) + \nabla\cdot(\rho\vec{u}\vec{u}) = -\nabla p + \nabla\cdot\left[\mu\left(\nabla\vec{u} + \nabla\vec{u}^T\right)\right] + \rho\vec{g} + \vec{F}_{vol} \tag{8}$$

and

$$\frac{\partial}{\partial t}(\rho E) + \nabla\cdot[\vec{u}(\rho E + p)] = \nabla\cdot(k_{eff}\nabla T) + Q. \tag{9}$$

Fluid properties are determined from the vapor and liquid properties, weighted by their volume fractions,

$$\rho = \alpha_f \rho_f + \alpha_g \rho_g, \tag{10a}$$

$$\mu = \alpha_f \mu_f + \alpha_g \mu_g \tag{10b}$$

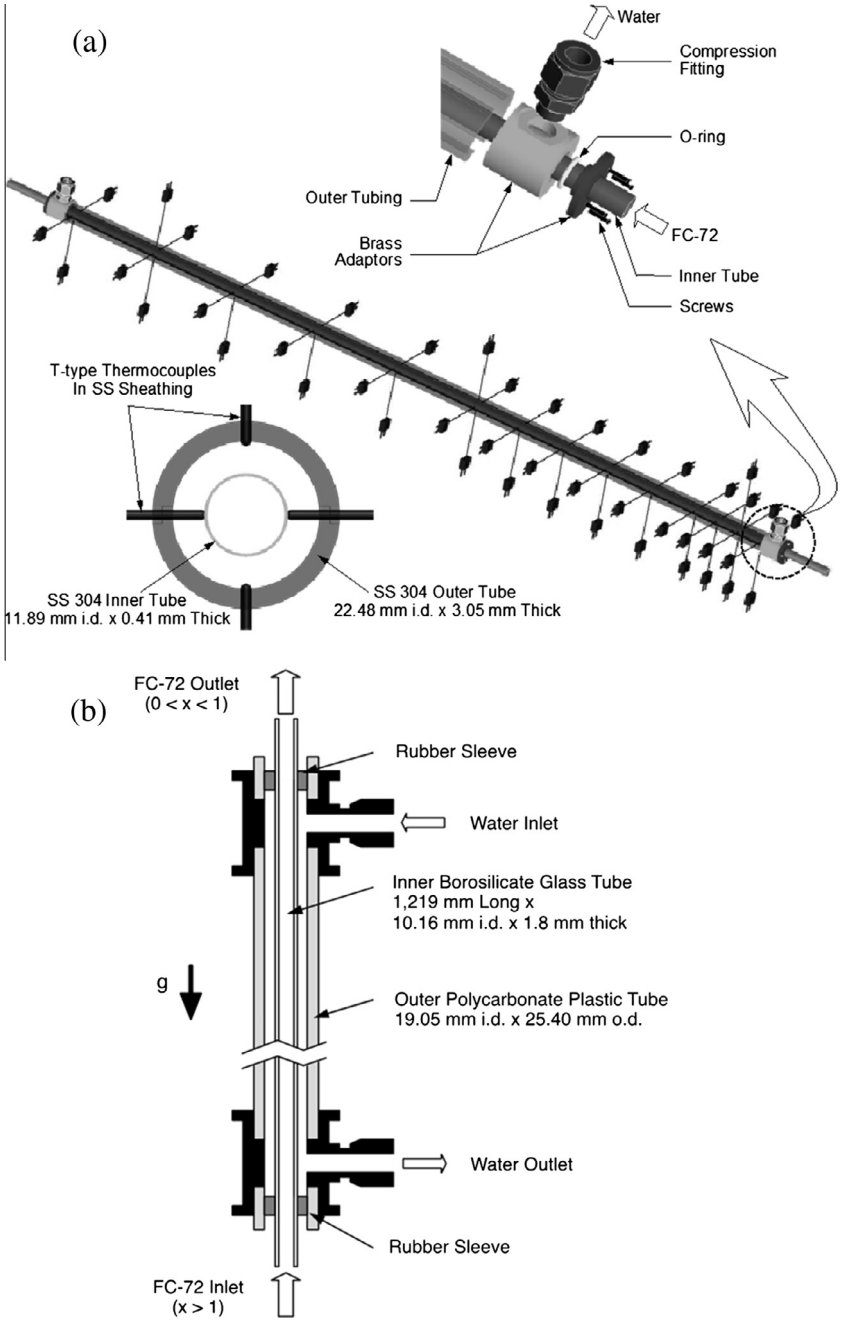

Fig. 2. (a) Condensation module for heat transfer measurements. (b) Condensation module for flow visualization.

Table 1
Operating conditions for the test cases from the experimental study also used in the computational simulation.

Test case	G (kg/m^2 s)	p_{in} (kPa)	T_{in} (K)	$x_{e,in}$	G_w (kg/m^2 s)	$T_{w,in}$ (°C)	$T_{w,out}$ (°C)	$q''_{wall,avg}$ (W/cm^2)
1	58.4	104.5	345.3	1.15	55.5	293.1	303.6	−2.15
2	116.7	108.0	347.7	1.16	92.5	294.4	303.4	−3.10
3	194.3	114.2	342.2	1.09	154.2	295.1	302.1	−3.85
4	271.5	124.6	345.0	1.09	215.8	295.1	301.6	−5.23

and

$$k_{eff} = \alpha_f k_f + \alpha_g k_g. \tag{10c}$$

The specific internal energy, E (J/kg), in Eq. (9) is determined as

$$E = \frac{\alpha_f \rho_f E_f + \alpha_g \rho_g E_g}{\alpha_f \rho_f + \alpha_g \rho_g}, \tag{11}$$

where $E_k = c_{v,k}(T - T_{sat})$. The volumetric mass source terms S_g and S_f in Eq. (7) are based on the Lee model [51], and given by Eqs. (6a) and (6b), respectively. A mass transfer intensity factor of $r_i = 10{,}000$ is assumed, which is based on a thorough assessment of the magnitude of this parameter by Lee et al. [25] for vertical downflow condensation. The energy source term due to phase change, Q (W/m^3), in Eq. (9) is determined as

$$Q = h_{fg} S_f. \tag{12}$$

The computational model accounts for vapor shear and the effects of surface tension and molecular viscosity at the film interface. The tangential and normal force equations at the film interface are given, respectively, by

$$e_{i,j}\vec{n}_j t_i = 0 \tag{13}$$

and

$$-p + 2\mu e_{i,j}\vec{n}_j t_i = \sigma\left(\frac{1}{R_1} + \frac{1}{R_2}\right). \tag{14}$$

Volume fraction gradients are used to calculate the curvature terms as per the continuum surface force model proposed by Brackbill et al. [54].

3.2. Computational domain and mesh size independence

Fig. 3(a) and (b) show the geometry adopted in modeling upflow annular condensation, and computational domain details, respectively. Fig. 3(b) also shows the boundary conditions used in the computational model. The flow is assumed axisymmetric and two-dimensional. The width of the domain is half the hydraulic diameter, $D_h/2 = 5.945$ mm, and the computational condensation length used is $L = 0.8$ m; this length is shorter than the actual length of the experimental test section as thermocouple measurements were only available up to $L = 0.8$ m. The actual length of the domain is set longer to avoid any end effects at the outlet. The mesh used has quadrilateral shape with uniform grid size in most of the domain, but with gradual refinement in a region adjacent to the condensing wall to accurately capture the formation of the liquid film and local turbulence as depicted in Fig. 3(b).

Fig. 4(a) shows computed values of the heat transfer coefficient spatially averaged over the region $0.2\text{ m} < z < 0.8\text{ m}$ for test case 4 in Table 1 corresponding to $G = 271.5\text{ kg/m}^2\text{ s}$, the highest mass velocity tested. The region $z < 0.2$ m is intentionally excluded from the averaging due to relatively poor prediction in the two-phase developing region by FLUENT as discussed later. Fig. 4(a) shows asymptotic values of the average heat transfer coefficient are realized for mesh sizes below about 10 μm. In the present study, a minimum size of $\Delta c = 2$ μm is used near the wall, which resulted in a minimum of five cells near the wall within $y^+ < 5$. For the same case of $G = 271.5\text{ kg/m}^2\text{ s}$, Fig. 4(b) shows the variation of wall y^+ (i.e., y^+ corresponding the first cell nearest to the wall) along the

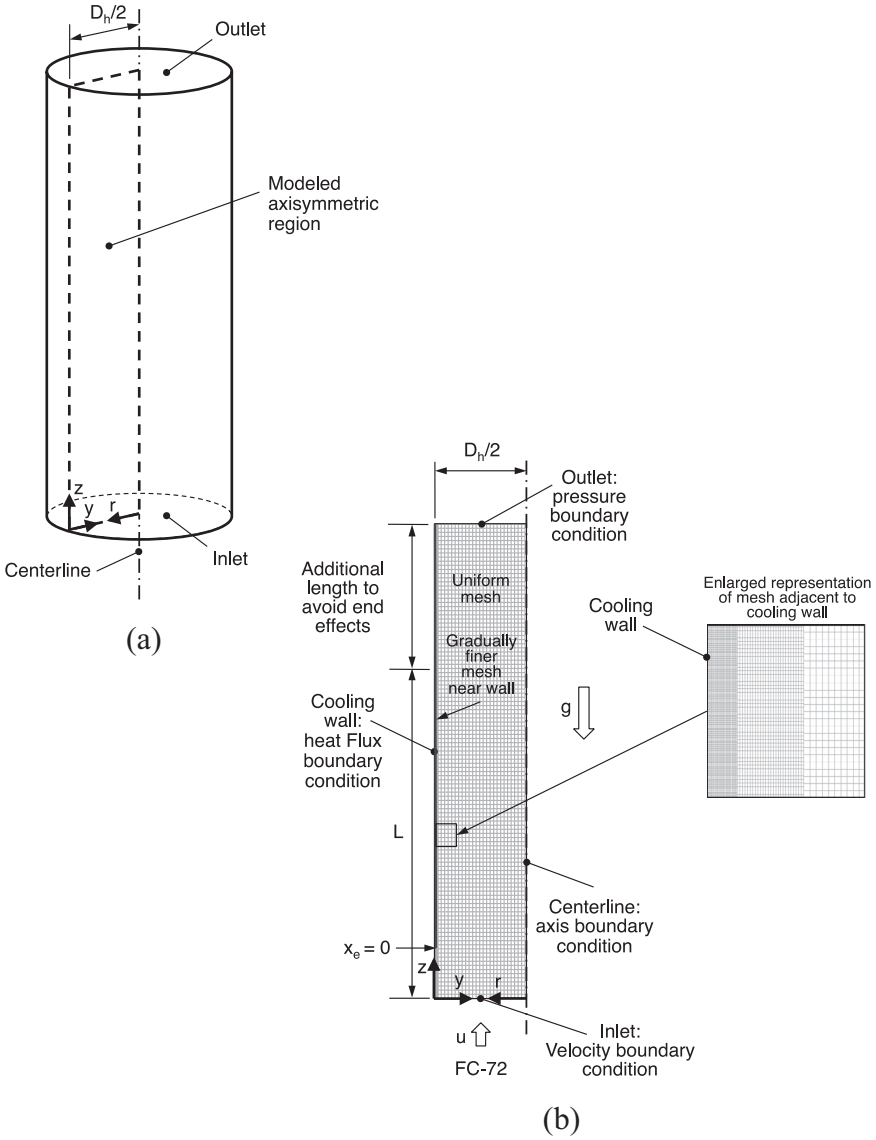

Fig. 3. (a) Cylindrical domain for the computational model. (b) 2-D axisymmetric domain modeled in the present study.

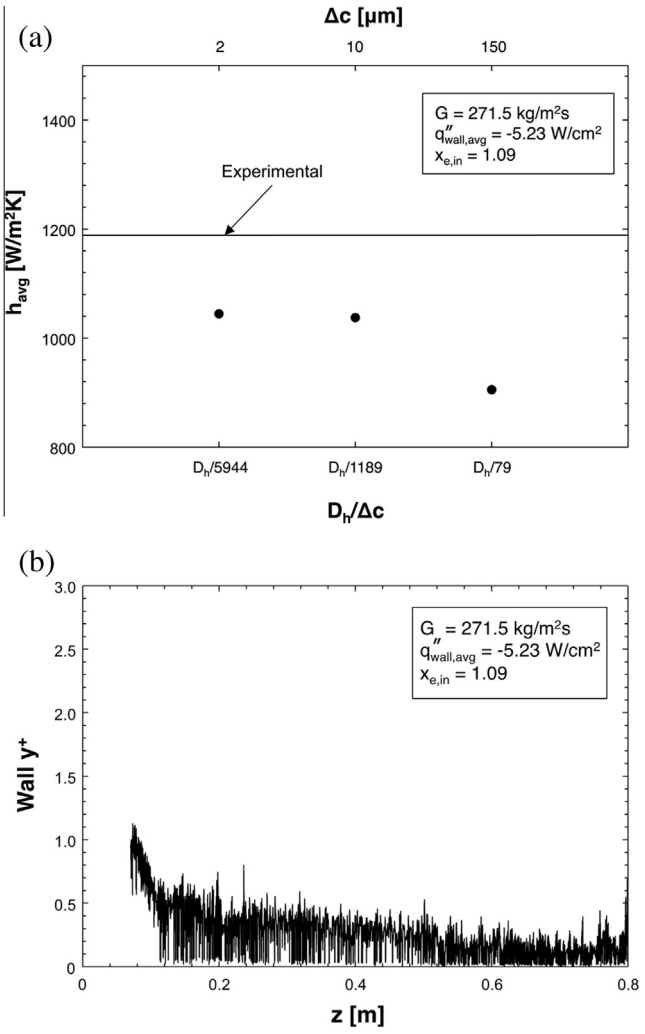

Fig. 4. (a) Analysis of grid independence based on spatially averaged condensation heat transfer coefficient. (b) Variation of wall y^+ along condensation length for test case 4 in Table 1.

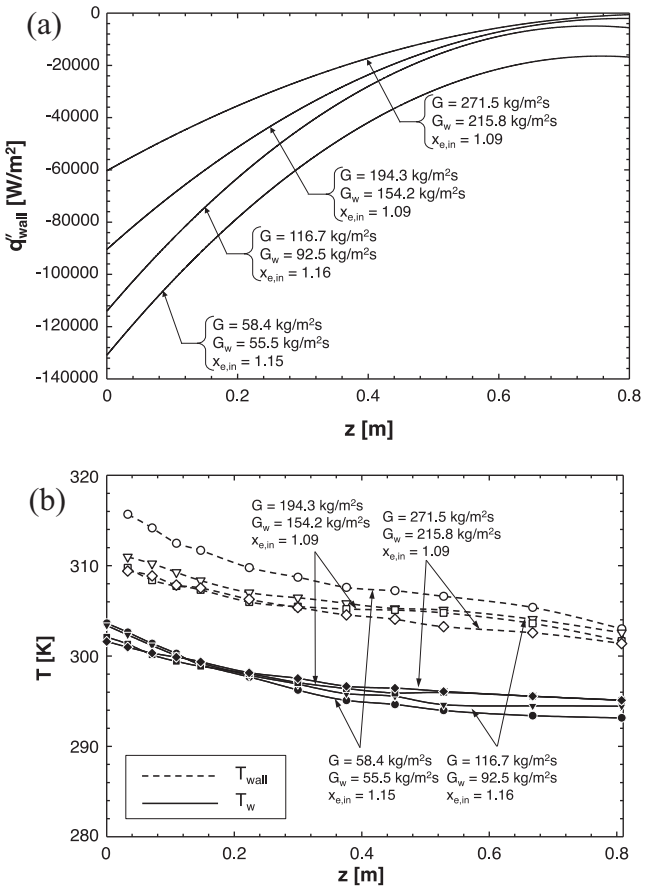

Fig. 5. Experimentally determined axial variations of (a) wall heat flux and (b) water temperature and outer wall temperature for four test conditions.

condensing length. The values shown are representative of wall y^+ values used to achieve convergence for all the operating conditions given in Table 1.

3.3. Initialization and boundary conditions

In both the experiments and computational model, FC-72 enters the circular channel as pure vapor superheated 9–16 °C, and inlet velocity is determined as $u = G/\rho_g$ based on inlet conditions provided in Table 1. Turbulence intensity, I, is estimated using the following formula derived from an empirical correlation for pipe flows [52]

$$I = \frac{u'}{\bar{u}} = 0.16(Re_{D_h})^{-1/8}. \tag{15}$$

The wall heat flux profile is provided as boundary condition at the wall using user defined functions (UDFs) in FLUENT. The wall heat flux is determined from the local differential sensible heat rise of the cooling water between consecutive waterside thermocouples,

$$q''_{wall} = \frac{\dot{m}_w c_{pw,f}(T_{w,i+1} - T_{w,i})}{\pi D_h (z_{i+1} - z_i)}. \tag{16}$$

Fig. 5(a) and (b) show, respectively, axial variations of the experimentally determined wall heat flux, and both water and wall temperatures for the four FC-72 mass velocities given in Table 1. Surface conditions consisting of roughness height, roughness constant and contact angle were set to default values of 0 m, 0.5 and 90°, respectively; a sensitivity study showed these parameters have minimal influence on computed values of the condensation heat transfer coefficient.

As indicated in a recent study by Lee et al. [25], it is very difficult to initiate a continuous liquid film in the upstream developing region of the flow channel. Following their computational technique, a very thin liquid film of thickness δ_i is initially applied from z_0 (where $x_e = 1$) along the entire condensation length to expedite convergence time. Applying this initial thickness to the entire condensation length is crucial for vertical upflow since the combination of a highly turbulent vapor core and gravity opposite to the flow direction would shear the film faster than with vertical downflow. Additionally, phase change models are incapable of predicting the location where liquid film is initiated. To overcome this difficulty, as suggested by Lee et al. an average liquid film thickness is obtained from an annular flow model [55] for the developing length between $z = z_0$ and $z = z_0 + 0.05$ m to determine δ_i. The location z_0 corresponding to $x_e = 1$ for each of the four test cases is determined from the simple energy balance

$$x_e = 1 + \frac{c_{p,g}(T_g - T_{sat})}{h_{fg}}. \tag{17}$$

The calculated initial liquid film thicknesses are in the range of $\delta_i = 35$–60 μm, which are less than 0.6% of the channel diameter. The computed convergent thickness is observed to be significantly greater than the initial thickness estimated from upstream conditions.

4. Computational results

4.1. Interfacial behavior

Interfacial waviness, liquid entrainment and liquid deposition are inherent features of annular flow condensation. Fig. 6(a) shows predicted interfacial behavior for $G = 271.5$ kg/m^2 s and a segment of the channel centered at $z = 590$ mm; individual images in the sequence are $\Delta t = 0.0004$ s apart. The predictions show complicated interfacial behavior in the liquid film along the wall. Waves in the film's interface generate small liquid masses that are first entrained into the vapor core and then deposited back upon the liquid film. Other interfacial features include liquid ligaments from the liquid film that are elongated, creating a necking region, before snapping and being pushed away from the wall. These latter features appear to possess sufficient radial momentum to be pushed towards the centerline rather than be re-deposited upon the wall liquid film. These features are captured in the circular areas in Fig. 6(a), where an elongated liquid protrusion is captured with an adjoining small liquid mass upstream. The small liquid mass is shown being quickly re-deposited upon the wall liquid film, while the liquid ligament jets forward and away from the wall, creating a necking region, before being pinched away and projected towards the centerline. The axisymmetric domain produces vapor

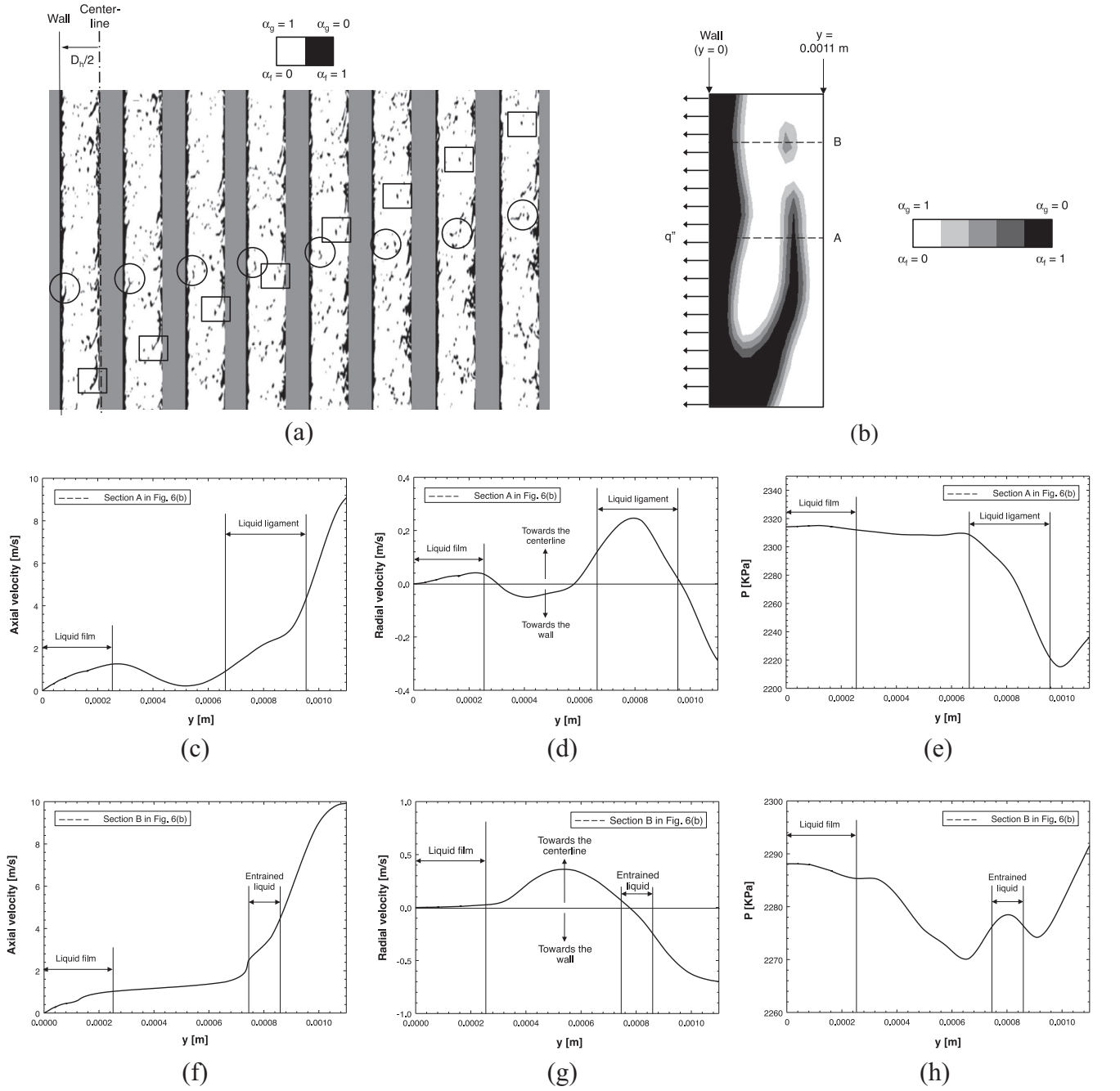

Fig. 6. (a) Computed sequential images of climbing film in outlet region centered at $z = 590$ mm for $G = 271.5$ kg/m^2 s and $G_w = 215.8$ kg/m^2 s; individual images in the sequence are separated by 0.0004 s. (b) Enlarged view of features in the circular area of the first image in (a). (c) Variation of axial velocity across section A in (b). (d) Variation of radial velocity across section A. (e) Variation of pressure across section A. (f) Variation of axial velocity across section B in (b). (g) Variation of radial velocity across section B. (h) Variation of pressure across section B.

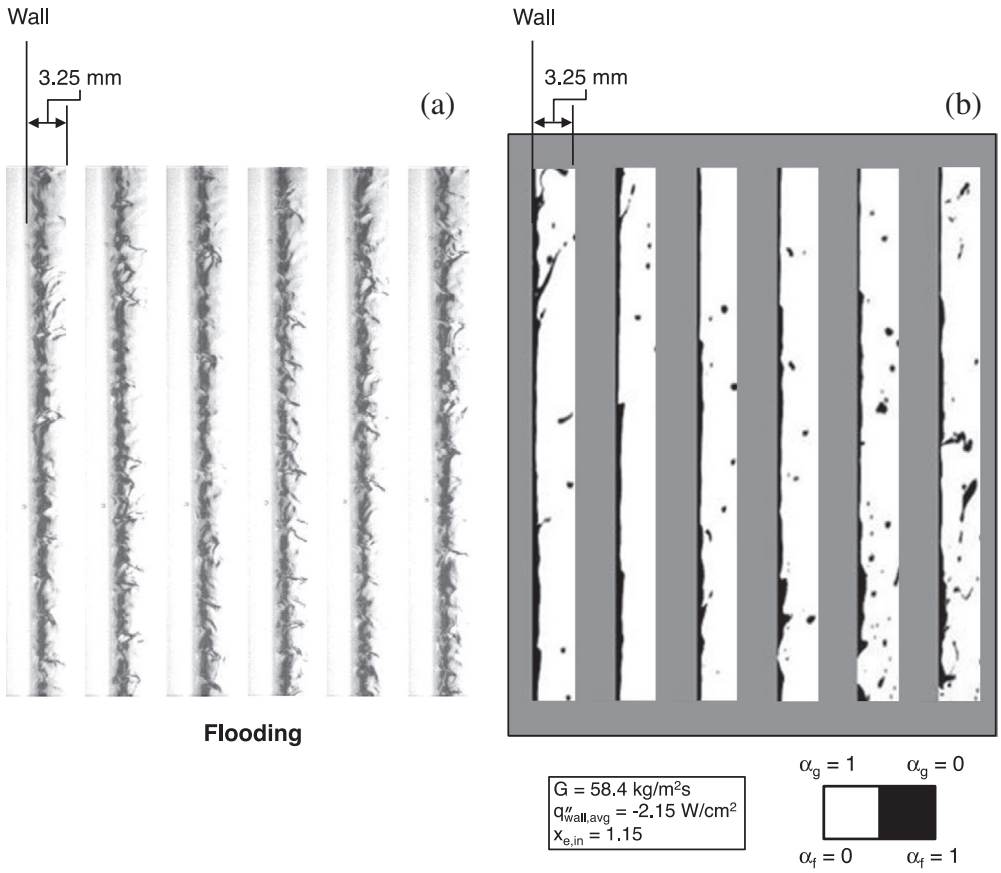

Fig. 7. (a) Experimentally obtained sequential images of liquid film in inlet region (centered at z = 190 mm) of flow visualization module with $G = 53.3$ kg/m^2 s and $G_w = 73.4$ kg/m^2 s corresponding to flooding conditions. (b) Computed sequential images of film at same axial location with $G = 58.4$ kg/m^2 s and $G_w = 55.5$ kg/m^2 s. Individual images in both sequences are separated by 0.0125 s.

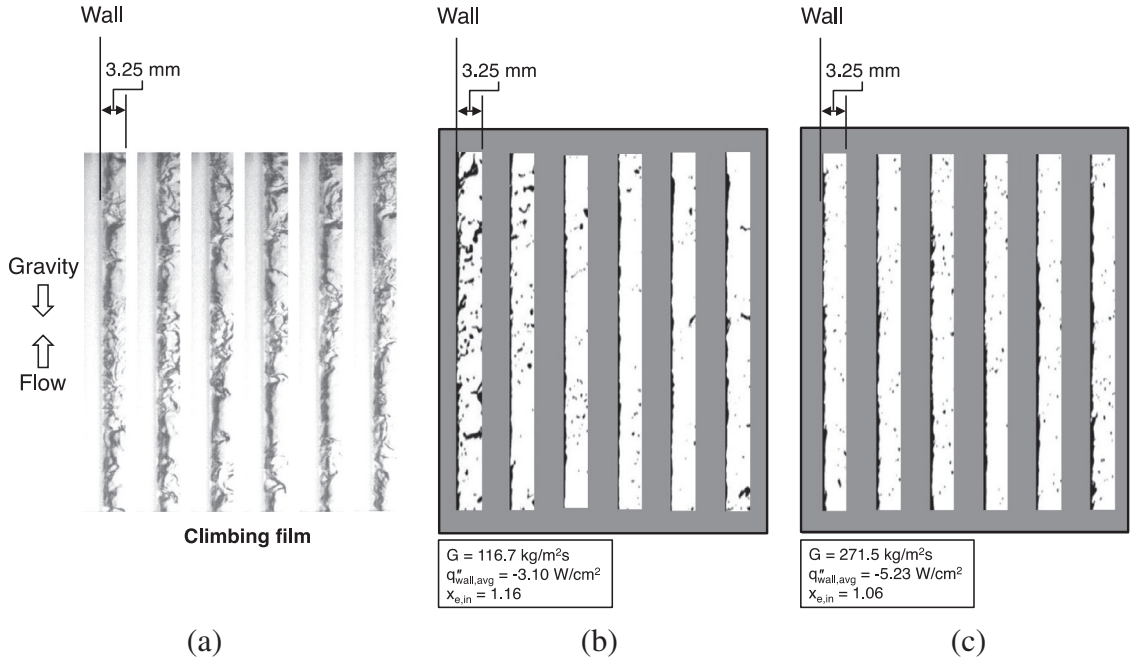

Fig. 8. (a) Experimentally obtained sequential images of liquid film in outlet region (centered at $z = 952$ mm) of flow visualization module with $G = 106.5$ kg/m^2 s and $G_w = 97.8$ kg/m^2 s corresponding to climbing film flow. (b) Computed sequential images of film in outlet region (centered at $z = 590$ mm) with $G = 116.7$ kg/m^2 s and $G_w = 92.5$ kg/m^2 s. (c) Computed sequential images of film in outlet region (centered at $z = 590$ mm) with $G = 271.5$ kg/m^2 s and $G_w = 215.8$ kg/m^2 s. Individual images in all three sequences are separated by 0.0125 s.

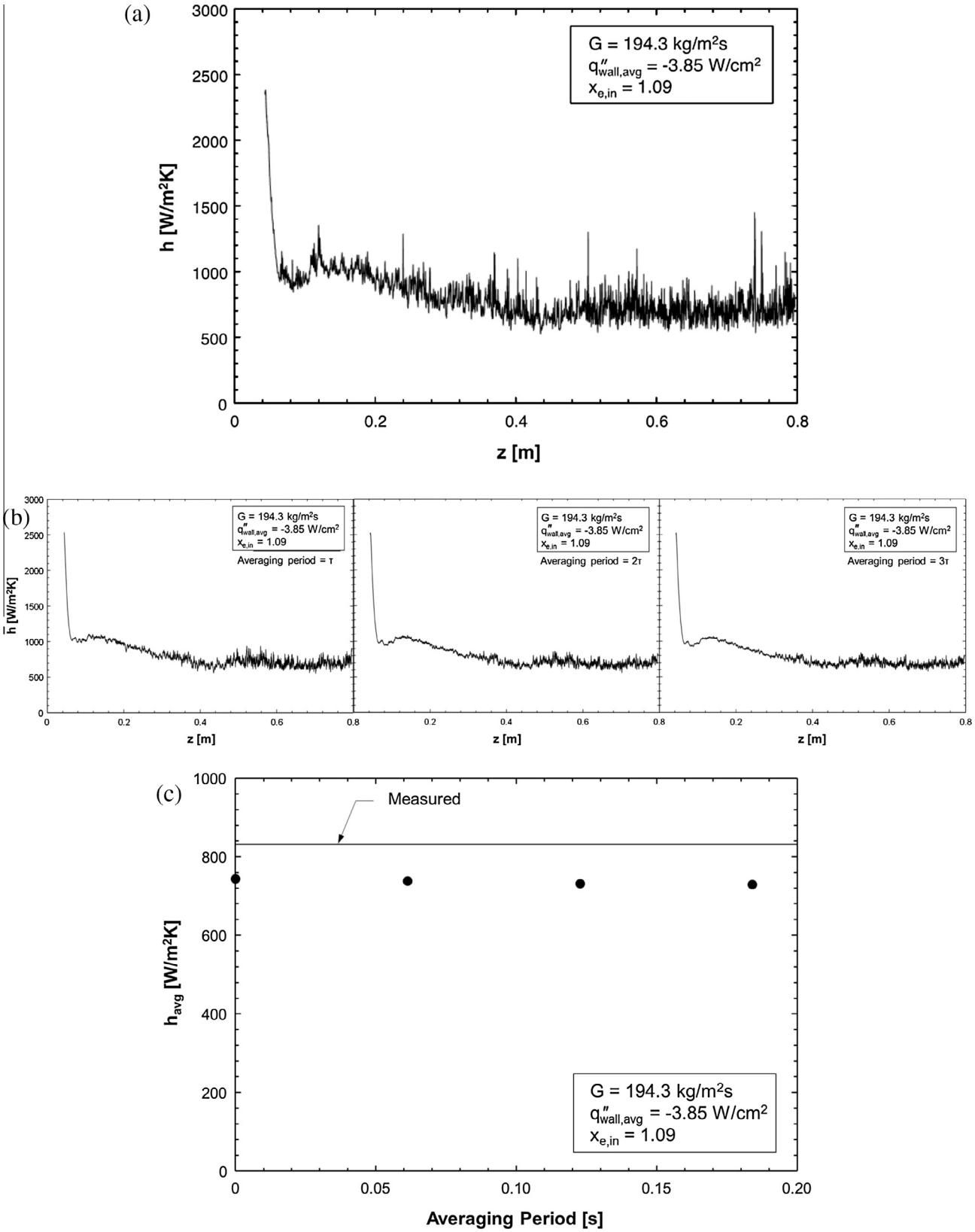

Fig. 9. (a) Axial variations of instantaneous computed local condensation heat transfer coefficients. (b) Axial variations of computed local condensation heat transfer coefficients averaged over different time periods. (c) Variation of average local heat transfer coefficients with averaging time period.

radial motion towards the centerline, causing liquid to accumulate around the centerline rather than be dispersed uniformly in the vapor core. The rectangular areas in Fig. 6(a) show liquid breaking away from the centerline region and being projected towards the wall. Overall, the present computations show both the wall and centerline are primary locations for liquid accumulation. Previous

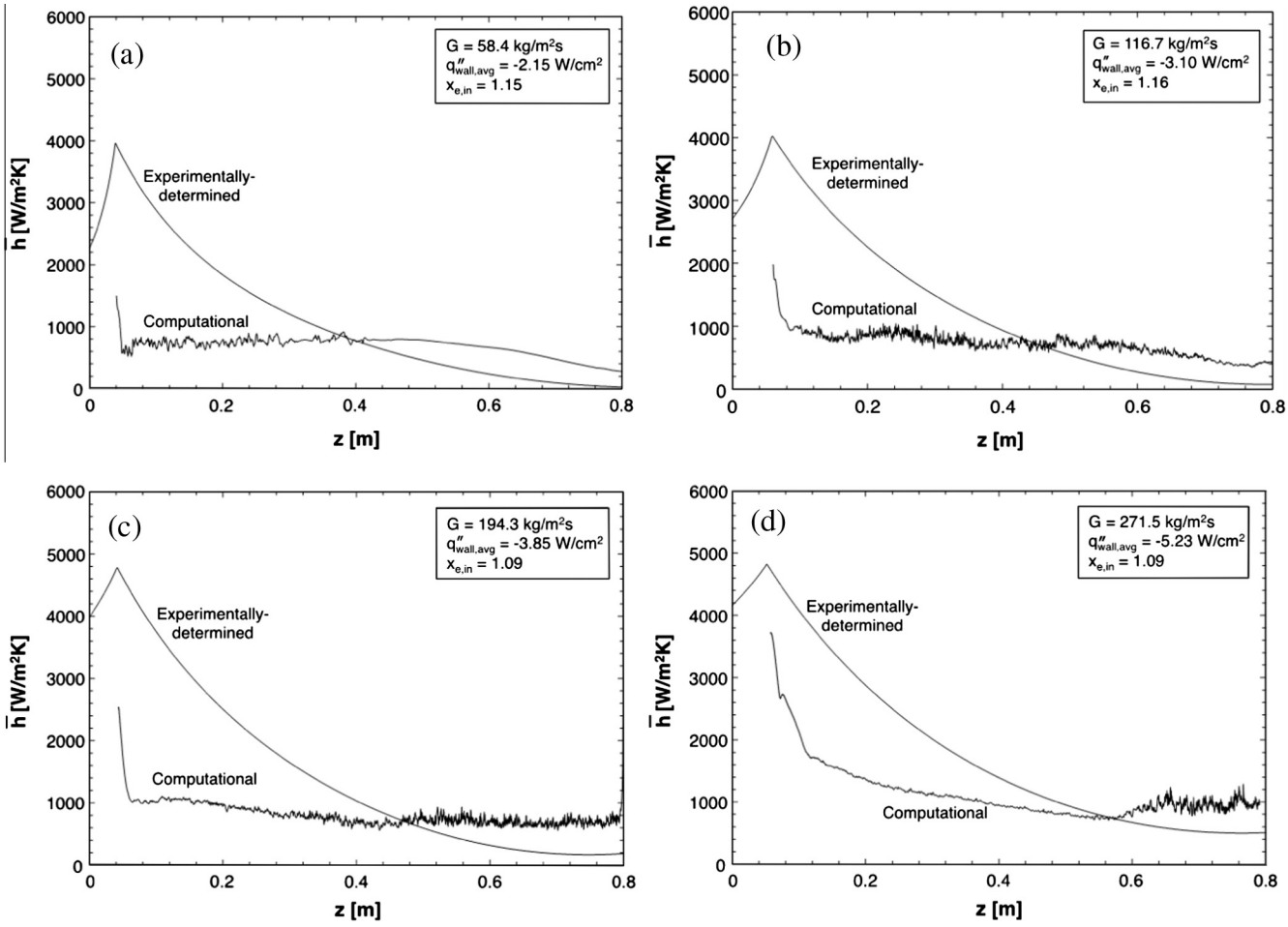

Fig. 10. Comparison of experimental and computed local condensation heat transfer coefficients for (a) $G = 58.4$ kg/m^2 s, (b) $G = 116.7$ kg/m^2 s, (c) $G = 194.3$ kg/m^2 s, and (d) $G = 271.5$ kg/m^2 s.

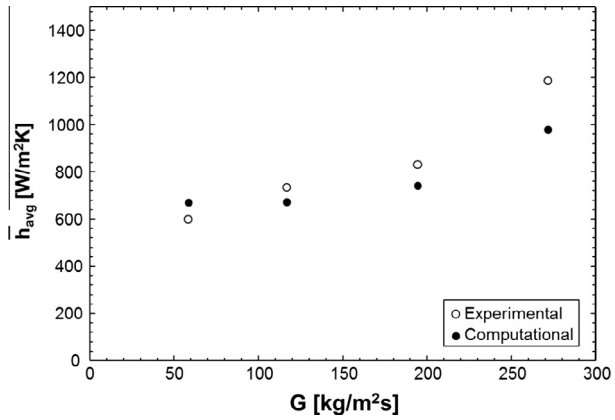

Fig. 11. Comparison of experimental and computed spatially averaged condensation heat transfer coefficient versus mass velocity.

studies on turbulent two-phase flow with entrained bubbles have shown a tendency of the bubbles to move away from the wall because of decreased effectiveness of bubble-induced skin friction drag reduction (BDR) [56]. In another study [57], numerical simulations of liquid droplets in turbulent vapor flow have shown a tendency of droplet migration away from the wall.

The near wall interfacial features discussed in the previous section are explained quantitatively using Fig. 6(b), which depicts an enlargement of features captured in the circular area within the first image in Fig. 6(a). Fig. 6(c)–(e) show local variations of axial velocity, radial velocity and pressure, respectively, across section A in Fig. 6(b), which includes the wall liquid film and extended liquid ligament. The axial velocity profile in Fig. 6(c) shows the liquid ligament lying in the relatively high velocity region of the turbulent vapor core. Fig. 6(d) shows the radial velocity of the liquid ligament is positive, indicating a tendency for the ligament to be projected towards the centerline. Fig. 6(e) shows pressure decreases across the liquid ligament, which is further evidence of the ligament tending to move away from the wall.

Fig. 6(f)–(h) show the local variations of axial velocity, radial velocity and pressure, respectively, across section B in Fig. 6(b), which includes the wall liquid film and small entrained liquid mass. The axial velocity profile in Fig. 6(f) shows this mass lying in the relatively high velocity region of the turbulent vapor core, similar to the ligament in section A. Fig. 6(g) shows the radial velocity of the liquid mass is close to zero but mostly negative, which implies a tendency to be deposited back upon the wall liquid film. Fig. 6(h) shows a local rise in pressure across the liquid mass within a region of mostly increasing pressure away from the wall, another indication of a tendency of this liquid to de deposited upon the wall liquid film.

Fig. 7(a) shows sequential images of FC-72 condensing along the inner wall of the glass tube of the flow visualization test module, centered at $z = 190$ mm, for $G = 53.3$ kg/m^2 s. Fig. 7(b) shows computed images at the same location for $G = 58.4$ kg/m^2 s, test

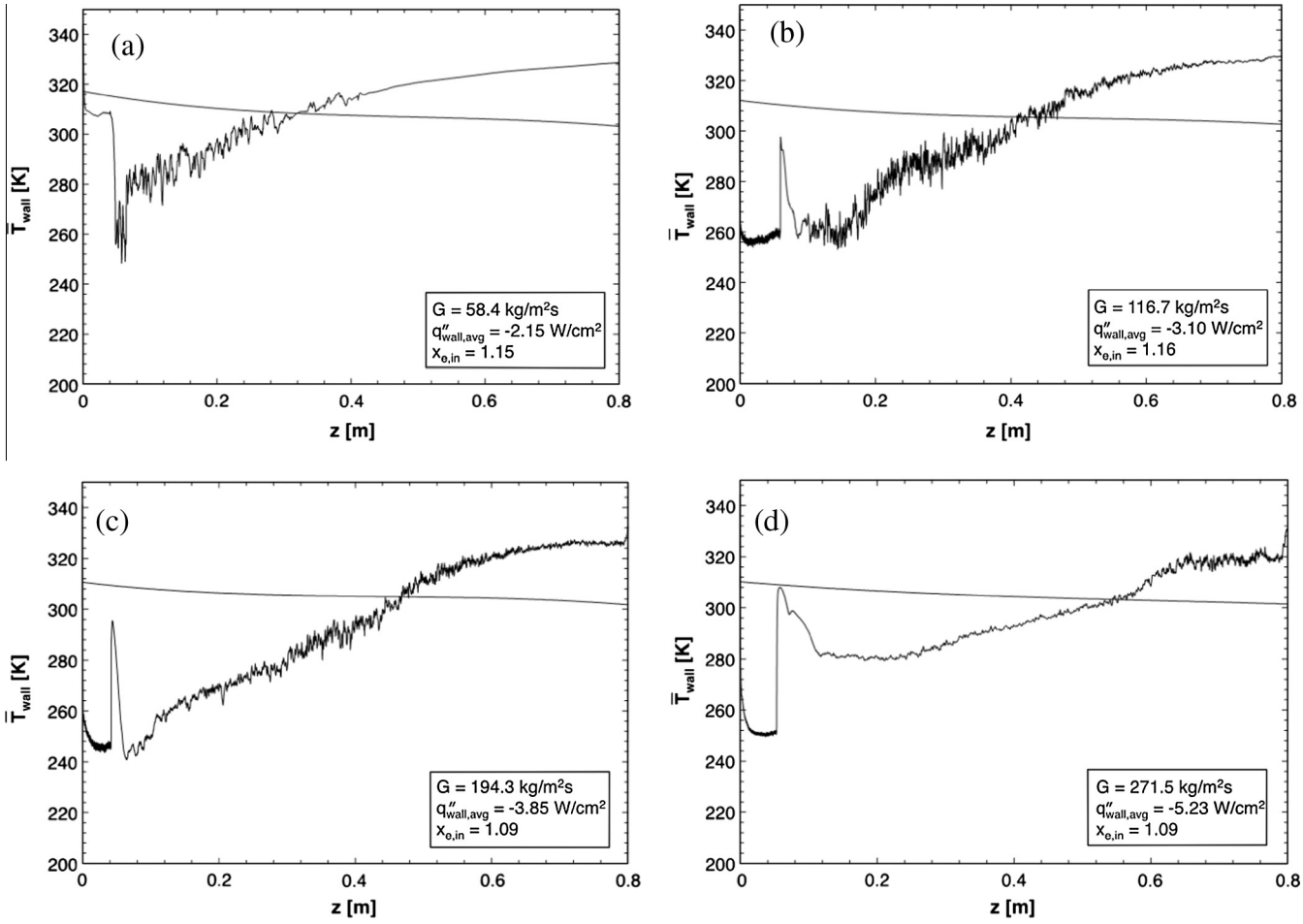

Fig. 12. Comparison of experimental and computed local wall temperature for (a) $G = 58.4$ kg/m^2 s, (b) $G = 116.7$ kg/m^2 s, (c) $G = 194.3$ kg/m^2 s, and (d) $G = 271.5$ kg/m^2 s.

case 1 in Table 1, obtained from the heat transfer measurements test module. As discussed by Park et al. [3], this condition is representative of the onset of *flooding* according to the Wallis relation [58]. The interface in the flow visualization sequence shows the liquid film exhibiting a combination of small ripples and large waves, with liquid ligaments emanating towards the centerline. The computational images show mostly large waves with liquid ligaments, with smaller ripples superimposed on the large waves.

Fig. 8(a) shows sequential images of FC-72 condensing along the inner wall of the glass tube of the flow visualization test module, centered at $z = 987$ mm, for $G = 106.5$ kg/m^2 s, which correspond to *climbing film* conditions, as indicated by Park et al. [3]. Because heat flux data from the heat transfer measurements module that are used as boundary condition for the computations are only available up to the last thermocouple location at $z = 0.80$ m, it is impossible to directly compare computed versus flow visualization results for $z = 987$ mm. However, conditions upstream of $z = 0.80$ m are also associated with climbing film conditions [3]. Fig. 8(b) and (c) show computed images for $G = 116.7$ and 271.5 kg/m^2 s, respectively, centered at $z = 590$ mm. Both experimental results, Fig. 8(a), and computed results, Fig. 8(b) and (c), show shear driven flow with the liquid film flowing firmly upwards, with both interfacial ripples and small liquid masses entrained in the vapor core.

4.2. Heat transfer results

Fig. 9(a) shows the computed instantaneous variation of the heat transfer coefficient along the flow direction for $G = 194.3$ kg/m^2 s. Notice the large local fluctuations, given the complex interfacial behavior of the thin annular film. These fluctuations are extremely difficult to capture experimentally because of wall temperature dampening provided by the thermal mass of the stainless steel tube. In recent computational studies involving sensible heating [59] and evaporative heating [53] of turbulent free-falling water films, heat transfer plots were comparatively smoother. While free-falling films also exhibit complex interfacial waviness, any wall temperature fluctuations resulting from these waves are greatly reduced by the relatively large thickness of a free-falling film compared to the much smaller thickness of a shear-driven film in annular condensing flows. Interfacial waves in the latter are felt immediately at the wall, while waves in falling films are more remote from the wall.

Hence, it is important to assess the significance of the relatively large fluctuations in Fig. 9(a) by time-averaging the computed heat transfer coefficient results. An averaging time period is defined as

$$\tau = \frac{L}{U_{g,in}}, \tag{18}$$

where $L = 0.8$ m is the modeled condensation length and $U_{g,in}$ the inlet vapor velocity of the superheated FC-72. The local condensation heat transfer coefficient is averaged over period τ according to relation

$$\bar{h}(z) = \frac{1}{\tau}\int_0^{\tau} h(z,t)dt. \tag{19}$$

Fig. 9(b) shows heat transfer coefficient plots averaged over periods τ, 2τ and 3τ. Notice the gradual decline in fluctuations that result

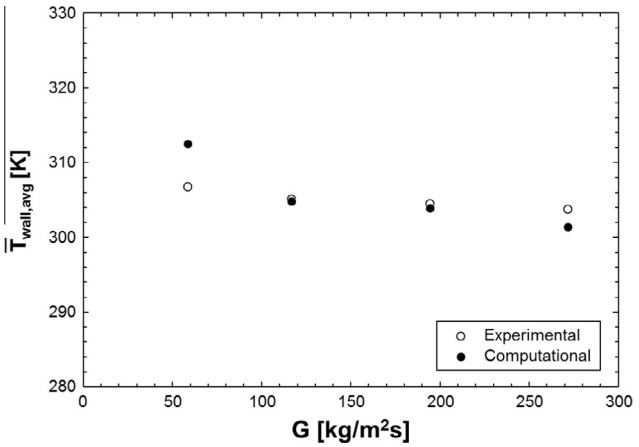

Fig. 13. Comparison of experimental and computed spatially averaged wall temperature versus mass velocity.

from increasing the averaging period. Fig. 9(c) shows the spatial average of the heat transfer coefficient over the region 0.2 m < z < 0.8 m is fairly insensitive to averaging period. This proves that the spatial average of the heat transfer coefficient is captured quite consistently, even on an instantaneous basis. This is especially important given the large computational time required to compute an average over a very long period.

Fig. 10(a)–(d) compare axial variations of the computed local condensation heat transfer coefficient, time-averaged over period τ, to experimentally-determined variations for four FC-72 mass velocities of G = 58.4, 116.7, 194.3, and 271.5 kg/m^2 s, respectively. As indicated earlier, the computations are initiated where x_e = 1 rather than the superheated inlet. Overall, there is fair agreement in the downstream region but not the inlet region. Additionally, predictions in the downstream region appear to improve with increasing mass velocity, with G = 271.5 kg/m^2 s showing the best downstream agreement. Overall, local values are under-predicted upstream and over-predicted downstream for all mass velocities. The deviation between the experimental and computational results can be attributed to the inability of the computational model to accurately capture film thickness and turbulence in the inlet region, while doing a better job as the film gets thicker. In the inlet region, as discussed earlier, the phase change model is not able to initiate the liquid film, leading the authors to use an initial film thickness, δ_i, which affects the accuracy in this region. Nonetheless, the computational model is able to capture the spatially averaged measured values over the region 0.2 m < z < 0.8 m quite well as shown in Fig. 11.

4.3. Wall and film temperature results

Fig. 12(a)–(d) compare axial variations of computed local time-averaged wall temperature with experimental data for G = 58.4, 116.7, 194.3, and 271.5 kg/m^2 s, respectively. The time-averaging

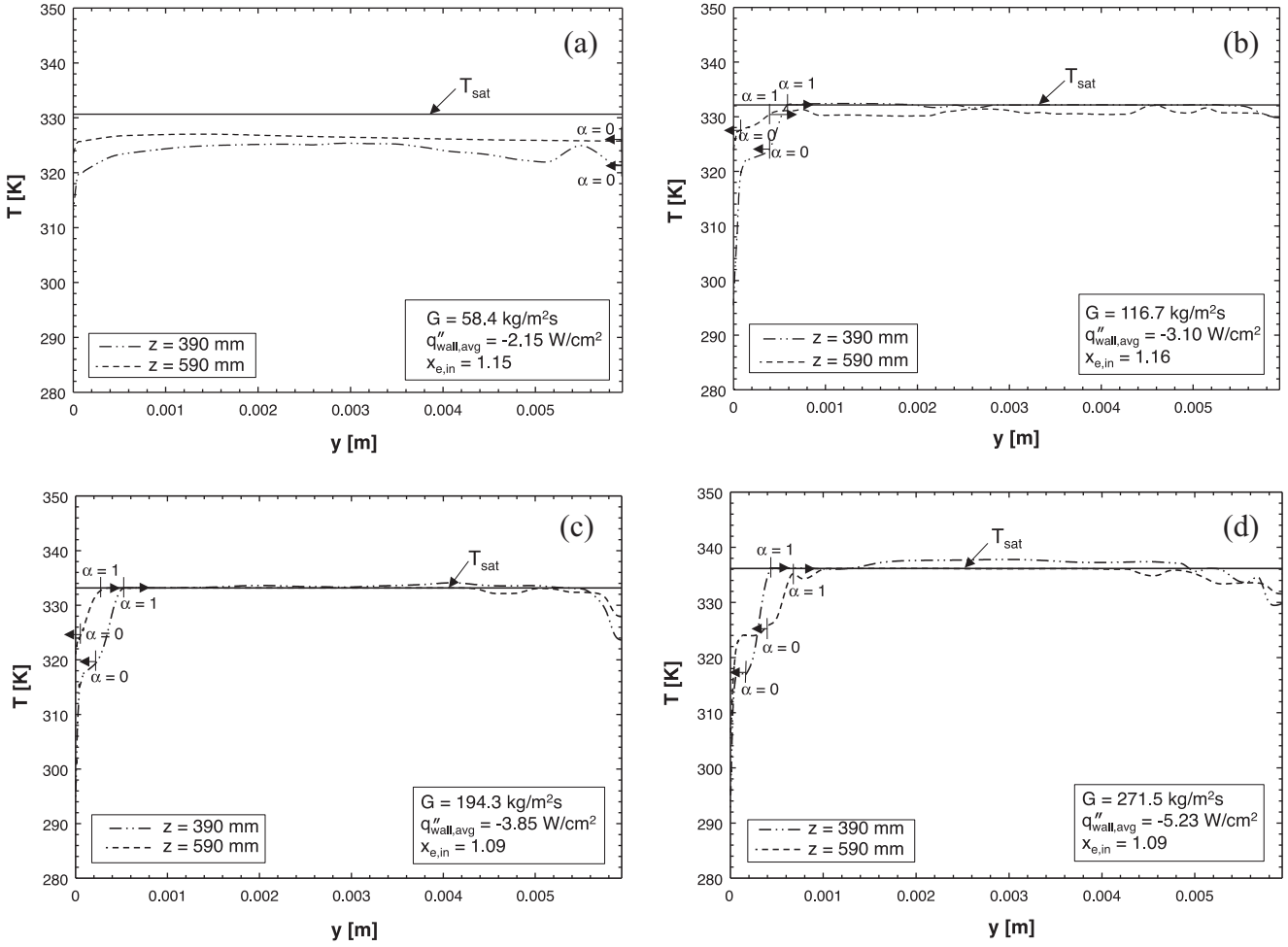

Fig. 14. Variation of computed fluid temperature with radial distance from the wall at two axial locations for (a) G = 58.4 kg/m^2 s, (b) G = 116.7 kg/m^2 s, (c) G = 194.3 kg/m^2 s, and (d) G = 271.5 kg/m^2 s.

period is the same as that used for the heat transfer plots in Fig. 10 (a)–(d). For all four cases, the experimental wall temperatures exhibit an almost linear decline with z, while the computational result feature more significant variations, which under-predict the data upstream and over-predict downstream. When compared to the experimental data, predicted wall temperatures are seen to increase along the channel. The under prediction of heat transfer data in the inlet region and improvement in the downstream region, as discussed earlier, cause a similar trend in the predicted wall temperatures. However, as shown in Fig. 13, the computational model shows good accuracy in capturing the spatially averaged measured wall temperatures over the region 0.2 m < z < 0.8 m.

Fig. 14(a)–(d) show, for G = 58.4, 116.7, 194.3, and 271.5 kg/m^2 s, respectively, temperature variations across the liquid and vapor phases at two axial locations of z = 390 and 590 mm. For the lowest flow rate of G = 58.4 kg/m^2 s, Fig. 14(a), almost the entire cross-section is covered with liquid at both axial locations. Once the flow has changed phase completely to liquid, no more mass transfer can occur as heat is being extracted from the FC-72, which is why the saturation temperature is not achieved across the channel for this lowest mass velocity. Predicting complete phase change to liquid can also be in part a result of the mass intensity factor of r_i = 10,000 being too high for this low mass velocity. In both axial locations of z = 390 and 590 mm, the interfacial temperature for all three higher mass velocities of G = 116.7, 194.3 and 271.5 kg/m^2 s is maintained within only ±3 °C of saturation temperature. Also for the same three mass velocities, there is an appreciable temperature drop across the liquid–vapor interface. Predicting a temperature across the vapor core close to saturation and capturing a temperature drop at the interface are both crucial to validating the phase change model. These same interfacial temperature trends were captured in recent studies by Kharangate et al. [53] and Lee et al. [25] to validate phase change models for falling film evaporation and downflow condensation, respectively. Kharangate et al. reasoned that the large temperature drop across the liquid film interface is caused by interfacial dampening of eddy diffusivity due to surface tension. The temperature is seen to drop near the center of the channel and is lower than saturation temperature. As discussed in relation to Fig. 6, this is caused by entrained liquid from the wall, where the temperature is lower than saturation, tending towards the center of the channel.

4.4. Future work

Clearly, the present computational model should be improved to more accurately capture liquid entrainment into the vapor core, and reduce the appreciable accumulation of liquid towards the centerline predicted by the present model. These improvements may be achieved by switching from 2-D to 3-D modeling, which has been attempted in a few prior studies [23,24]. Better model validation may also be achieved with better diagnostic measurements, such as simultaneous temperature and interfacial wave measurements [60], as well as the use of micro-particle image velocimetry (μ-PIV) [61] to measure velocity profile within the wall liquid film.

5. Conclusions

This study explored condensation of FC-72 in vertical upflow both experimentally and computationally. The computational model incorporates Lee's phase change model [51] in FLUENT and is used to predict variations of void fraction, condensation heat transfer coefficient, wall temperature and temperature profile across the liquid film. The key findings from the study are as follows.

(1) The computational model is capable of capturing the observed complex flow behavior across the condensing tube, including interfacial waviness, liquid entrainment in the vapor core and liquid deposition upon the film corresponding to flooding and climbing film conditions.
(2) The model under-predicts the local measured condensation heat transfer coefficient in the upstream region of the condensation tube and over-predicts downstream. However, the measured spatially averaged condensation heat transfer coefficient is captured with good accuracy.
(3) The model also under-predicts the local measured wall temperature in the upstream region of the condensation tube and over-predicts downstream. Nonetheless, the measured spatially averaged wall temperature is predicted quite accurately.
(4) Predicted film temperature profiles show an appreciable temperature gradient at the liquid–vapor interface while also maintaining saturation temperature in the vapor core, which help validate the effectiveness of Lee's phase change model [51] in capturing interfacial mass transfer.
(5) Further enhancement of predictive accuracy will require switching from 2-D to 3-D modeling. Equally important is the need for more sophisticated diagnostic tools to measure velocity field and temperature within the wall liquid film, as well as map the film's interfacial waviness.

Acknowledgement

The authors are grateful for the support of this Project by the National Aeronautics and Space Administration (NASA) under Grant No. NNX13AB01G.

References

[1] I. Mudawar, Two-phase micro-channel heat sinks: theory, applications and limitations, J. Electron. Packag. Trans. ASME 133 (2011). 041002-2.
[2] I. Park, S. Kim, I. Mudawar, Experimental measurement and modeling of downflow condensation in a circular tube, Int. J. Heat Mass Transfer 57 (2013) 567–581.
[3] I. Park, I. Mudawar, Climbing film, flooding and falling film behavior in upflow condensation in tubes, Int. J. Heat Mass Transfer 65 (2013) 44–61.
[4] S.M. Kim, J. Kim, I. Mudawar, Flow condensation in parallel micro-channels – Part 1: experimental results and assessment of pressure drop correlations, Int. J. Heat Mass Transfer 55 (2012) 971–983.
[5] H.M. Soliman, The mist-annular transition during condensation and its influence on the heat transfer mechanism, Int. J. Multiphase Flow 12 (1986) 277–288.
[6] H.M. Soliman, On the annular-to-wavy flow pattern transition during condensation inside horizontal tubes, Can. J. Chem. Eng. 60 (1982) 475–481.
[7] Q. Chen, R.S. Amano, M. Xin, Experimental study of flow patterns and regimes of condensation in horizontal three-dimensional micro-fin tubes, Int. J. Heat Mass Transfer 43 (2006) 201–206.
[8] S.M. Kim, I. Mudawar, Flow condensation in parallel micro-channels. Part 2: heat transfer results and correlation technique, Int. J. Heat Mass Transfer 55 (2012) 984–994.
[9] X. Huang, G. Ding, H. Hu, Y. Zhu, H. Peng, Y. Gao, B. Deng, Influence of oil on flow condensation heat transfer of R410A inside 4.18 mm and 1.6 mm inner diameter horizontal smooth tubes, Int. J. Refrig. 33 (2010) 158–169.
[10] J.E. Park, F. Vakili-Farahani, L. Consolini, J.R. Thome, Experimental study on condensation heat transfer in vertical minichannels for new refrigerant R1234ze(E) versus R134a and R236fa, Exp. Therm. Fluid Sci. 35 (2011) 442–454.
[11] W.W. Akers, H.F. Rosson, Condensation inside a horizontal tube, Chem. Eng. Prog. Symp. 56 (1960) 145–149.
[12] A. Cavallini, R. Zecchin, A dimensionless correlation for heat transfer in forced convection condensation, in: Proceedings of 5th International Heat Transfer Conference, vol. 3, Tyoko, Japan, 1974, pp. 309–313.
[13] M.M. Shah, A general correlation for heat transfer during film condensation inside pipes, Int. J. Heat Mass Transfer 22 (1979) 547–556.
[14] H. Haraguchi, S. Koyama, T. Fujii, Condensation of refrigerants HCFC 22, HFC 134a and HCFC 123 in a horizontal smooth tube (2nd report), Trans. JSME (B) 60 (1994) 245–252.
[15] M.K. Dobson, J.C. Chato, Condensation in smooth horizontal tubes, J. Heat Transfer Trans. ASME 120 (1998) 193–213.

[16] K.W. Moser, R.L. Webb, B. Na, A new equivalent Reynolds number model for condensation in smooth tubes, J. Heat Transfer Trans. ASME 120 (1998) 410–417.
[17] W.W. Wang, T.D. Radcliff, R.N. Christensen, A condensation heat transfer correlation for millimeter-scale tubing with flow regime transition, Exp. Therm. Fluid Sci. 26 (2002) 473–485.
[18] S. Koyama, K. Kuwahara, K. Nakashita, K. Yamamoto, An experimental study on condensation of refrigerant R134a in a multi-port extruded tube, Int. J. Refrig. 24 (2003) 425–432.
[19] M.M. Shah, An improved and extended general correlation for heat transfer during condensation in plain tubes, HVAC&R Res. 15 (2009) 889–913.
[20] T. Bohdal, H. Charun, M. Sikora, Comparative investigations of the condensation of R134a and R404A refrigerants in pipe minichannels, Int. J. Heat Mass Transfer 54 (2011) 1963–1974.
[21] S.M. Kim, I. Mudawar, Theoretical model for annular flow condensation in rectangular micro-channels, Int. J. Heat Mass Transfer 55 (2012) 958–970.
[22] H. Ganapathy, A. Shooshtari, K. Choo, S. Dessiatoun, M. Alshehhi, M. Ohadi, Volume of fluid-based numerical modeling of condensation heat transfer and fluid flow characteristics in microchannels, Int. J. Heat Mass Transfer 65 (2013) 62–72.
[23] E.D. Riva, D.D. Col, Effect of gravity during condensation of R134a in a circular minichannel, Microgravity Sci. Technol. 23 (2011) 87–97.
[24] S. Chen, Z. Yang, Y. Duan, Y. Chen, D. Wu, Simulation of condensation flow in a rectangular microchannel, Chem. Eng. Process. Process Intensification 76 (2014) 60–69.
[25] H. Lee, C.R. Kharangate, N. Mascharehnas, I. Park, I. Mudawar, Experimental and computational investigation of vertical downflow condensation, Int. J. Heat Mass Transfer 85 (2015) 865–879.
[26] R.A. Gingold, J.J. Monaghan, Smoothed particle hydrodynamics: theory and application to non-spherical stars, Mon. Notes R. Astron. Soc. 181 (1977) 375–389.
[27] L.B. Lucy, A numerical approach to the testing of the fission hypothesis, Astron. J. 82 (1977) 1013–1024.
[28] F.H. Harlow, A machine calculation method for hydrodynamic problems, Los Alamos Scientific Laboratory Report LAMS-1956, 1955.
[29] S. Osher, J.A. Sethian, Fronts propagating with curvature dependent speed: algorithms based on Hamilton–Jacobi formulations, J. Comput. Phys. 79 (1988) 12–49.
[30] C.W. Hirt, B.D. Nichols, Volume of fluid (VOF) method for the dynamics of free boundary, J. Comput. Phys. 39 (1981) 201–225.
[31] M. Sussman, E.G. Puckett, A coupled level set and volume-of-fluid method for computing 3D and axisymmetric incompressible two-phase flows, J. Comput. Phys. 162 (2000) 301–337.
[32] D. Enright, R. Fedkiw, J. Ferziger, I. Mitchell, A hybrid particle level set method for improved interface capturing, J. Comput. Phys. 183 (2002) 83–116.
[33] G. Tomar, G. Biswas, A. Sharma, A. Agrawal, Numerical simulation of bubble growth in film boiling using a coupled level-set and volume-of-fluid method, Phys. Fluids 17 (2005) 112103.
[34] S.O. Unverdi, G. Tryggvason, A front-tracking method for viscous, incompressible, multi-fluid flows, J. Comput. Phys. 100 (1992) 25–37.
[35] G. Tryggvason, B. Bunner, A. Esmaeeli, D. Juric, N. Al-Rawahi, W. Tauber, J. Han, S. Nas, Y.-J. Jan, A front-tracking method for the computations of multiphase flow, J. Comput. Phys. 169 (2001) 708–759.
[36] J.A. Shmerler, I. Mudawar, Local heat transfer coefficient in wavy free-falling turbulent liquid films undergoing uniform sensible heating, Int. J. Heat Mass Transfer 31 (1988) 67–77.
[37] J.A. Shmerler, I. Mudawar, Local evaporative heat transfer coefficient in turbulent free-falling liquid films, Int. J. Heat Mass Transfer 31 (1988) 731–742.
[38] I. Mudawar, A.H. Howard, C.O. Gersey, An analytical model for near-saturated pool boiling CHF on vertical surfaces, Int. J. Heat Mass Transfer 40 (1997) 2327–2339.
[39] J.C. Sturgis, I. Mudawar, Critical heat flux in a long, rectangular channel subjected to one-sided heating – II. Analysis of CHF data, Int. J. Heat Mass Transfer 42 (1999) 1849–1862.
[40] D.D. Hall, I. Mudawar, Ultra-high critical heat flux (CHF) for subcooled water flow boiling – II. High-CHF database and design parameters, Int. J. Heat Mass Transfer 42 (1999) 1429–1456.
[41] S. Mukherjee, I. Mudawar, Smart pumpless loop for micro-channel electronic cooling using flat and enhanced surfaces, IEEE Trans. CPMT Compon. Packag. Technol. 26 (2003) 99–109.
[42] D.C. Wadsworth, I. Mudawar, Enhancement of single-phase heat transfer and critical heat flux from an ultra-high-flux simulated microelectronic heat source to a rectangular impinging jet of dielectric liquid, J. Heat Transfer Trans. ASME 114 (1992) 764–768.
[43] M.K. Sung, I. Mudawar, Experimental and numerical investigation of single-phase heat transfer using a hybrid jet impingement/micro-channel cooling scheme, Int. J. Heat Mass Transfer 49 (2006) 682–694.
[44] D.D. Hall, I. Mudawar, Experimental and numerical study of quenching complex-shaped metallic alloys with multiple, overlapping sprays, Int. J. Heat Mass Transfer 38 (1995) 1201–1216.
[45] M. Visaria, I. Mudawar, Theoretical and experimental study of the effects of spray inclination on two-phase spray cooling and critical heat flux, Int. J. Heat Mass Transfer 51 (2008) 2398–2410.
[46] F. Gibou, L. Chen, D. Nguyen, S. Banerjee, A level set based sharp interface method for the multiphase incompressible Navier–Stokes equations with phase change, J. Comput. Phys. 222 (2007) 536–555.
[47] M. Knudsen, The kinetic theory of gases. Some modern aspects, Methuen's Monographs on Physical Subjects, London, UK, 1934.
[48] R.W. Schrage, A Theoretical Study of Interphase Mass Transfer, Columbia University Press, New York, 1953.
[49] R. Marek, J. Straub, Analysis of the evaporation coefficient and the condensation coefficient of water, Int. J. Heat Mass Transfer 44 (2001) 39–53.
[50] I. Tanasawa, Advances in condensation heat transfer, in: J.P. Hartnett, T.F. Irvine (Eds.), Advances in Heat Transfer, Academic Press, San Diego, CA, 1991.
[51] W.H. Lee, A pressure iteration scheme for two-phase flow modeling, in: T.N. Veziroglu (Ed.), Multiphase Transport Fundamentals, Reactor Safety, Applications, vol. 1, Hemisphere Publishing, Washington, DC, 1980.
[52] ANSYS FLUENT 12.1 in Workbench User's Guide. ANSYS Inc., Canonsburg, PA, 2009.
[53] C.R. Kharangate, H. Lee, I. Mudawar, Computational modeling of turbulent evaporating falling films, Int. J. Heat Mass Transfer 81 (2015) 52–62.
[54] J.U. Brackbill, D.B. Kothe, C. Zemach, A continuum method for modeling surface tension, J. Comput. Phys. 100 (1992) 335–354.
[55] H. Lee, I. Mudawar, M.M. Hasan, Experimental and theoretical investigation of annular flow condensation in microgravity, Int. J. Heat Mass Transfer 61 (2013) 293–309.
[56] M. Mattson, K. Mahesh, Simulation of bubble migration in a turbulent boundary layer, Phys. Fluids 23 (2011) 045107.
[57] S. Mortazavi, G. Tryggvason, A numerical study of motion of drops in Poiseuille flow. Part 1. Lateral migration of one drop, J. Fluid Mech. 411 (2000) 325–350.
[58] G.B. Wallis, Flooding velocities for air and water in vertical tubes, No. AEEW-R-123, United Kingdom Atomic Energy Authority, Reactor Group, Atomic Energy Establishment, Winfrith, Dorset, England, 1961.
[59] N. Mascarehnas, I. Mudawar, Investigation of eddy diffusivity and heat transfer coefficient for free-falling turbulent liquid films subjected to sensible heating, Int. J. Heat Mass Transfer 64 (2013) 647–660.
[60] T.H. Lyu, I. Mudawar, Statistical investigation of the relationship between interfacial waviness and sensible heat transfer to a falling liquid film, Int. J. Heat Mass Transfer 34 (1991) 1451–1464.
[61] W. Qu, I. Mudawar, S.-Y. Lee, S.T. Wereley, Experimental and computational investigation of flow development and pressure drop in a rectangular micro-channel, J. Electron. Packag. Trans. ASME 128 (2006) 1–9.